Multiple single-element transducer photoacoustic computed tomography system

Sandeep Kumar Kalva, Zhe Zhi Hui, and Manojit Pramanik*
School of Chemical and Biomedical Engineering, Nanyang Technological University, 62 Nanyang Drive, Singapore 637459

ABSTRACT

Light absorption by the chromophores (hemoglobin, melanin, water etc.) present in any biological tissue results in local temperature rise. This rise in temperature results in generation of pressure waves due to the thermoelastic expansion of the tissue. In a circular scanning photoacoustic computed tomography (PACT) system, these pressure waves can be detected using a single-element ultrasound transducer (SUST) (while rotating in full 360^0 around the sample) or using a circular array transducer. SUST takes several minutes to acquire the PA data around the sample whereas the circular array transducer takes only a fraction of seconds. Hence, for real time imaging circular array transducers are preferred. However, these circular array transducers are custom made, expensive and not easily available in the market whereas SUSTs are cheap and readily available in the market. Using SUST for PACT systems is still cost effective. In order to reduce the scanning time to few seconds instead of using single SUST (rotating 360^0), multiple SUSTs can be used at the same time to acquire the PA data. This will reduce the scanning time by two-fold in case of two SUSTs (rotating 180^0) or by four-fold and eight-fold in case of four SUSTs (rotating 90^0) and eight SUSTs (rotating 45^0) respectively. Here we show that with multiple SUSTs, similar PA images (numerical and experimental phantom data) can be obtained as that of PA images obtained using single SUST.

Keywords: single element ultrasound transducer, multiple ultrasound transducers, photoacoustic tomography system, array transducers

1. INTRODUCTION

Photoacoustic imaging (PAI) is a hybrid biomedical imaging modality combining rich optical contrast and high ultrasonic resolution [1-8]. PAI works on the principle of photoacoustic effect. According to this phenomenon, when a pulsed laser beam is incident on any biological tissue, the chromophores present (such as blood, lipids, water etc.) absorb this light energy and the tissue gets heated up in the order of milli Kelvin. Due to the thermoelastic expansion of the tissue, photoacoustic (PA) waves are generated. These PA waves are detected by an ultrasound transducer around the sample. Several reconstruction methods can be used to map the initial pressure rise distribution with optical absorption in the tissue [9-17]. PA imaging has been employed for various applications such as small animal whole body imaging [18], molecular imaging [19], thyroid imaging [20], carotid imaging [21], sentinel lymph node imaging [22], tissue engineering [23], monitoring of blood oxygenation and deoxygenation levels [24] and so on [25, 26].

For deep-tissue imaging, circular scanning photoacoustic computed tomography (PAT/PACT) system is employed [27]. In this system, a single-element ultrasound transducer (SUST) collects the PA signals around the sample in full 2π rad. Usually, depending on the pulse repetition rate of the laser (Q-switched Nd:YAG laser [28]: 10-100 Hz; state-of-the-art PLD laser [29]: 7 KHz), SUST needs several minutes to few seconds for data acquisition. This impedes real-time monitoring of physiological changes that occur in fraction of seconds. Thus, to increase the temporal resolution of the PACT system, researchers are using circular-array transducers. State-of-the-art circular full-ring array transducer renders a very high frame rate of 50 Hz (each frame takes 0.02 sec) [3]. But this type of transducer is home-made and requires complex back-end parallel signal amplifiers and digitizers making them highly expensive. So, SUSTs are still

* Email: manojit@ntu.edu.sg

Photons Plus Ultrasound: Imaging and Sensing 2018, edited by Alexander A. Oraevsky, Lihong V. Wang, Proc. of SPIE Vol. 10494, 104944D · © 2018 SPIE · CCC code: 0277-786X/18/$18 · doi: 10.1117/12.2286606

preferred as they are cheap and readily available in the market. For high frame rates as that of full-ring array transducer based PACT systems, multiple SUSTs can be used.

If 'n' number of SUSTS are used in a multi-SUST PACT system, the data acquisition rate increases by n-fold as each SUST needs to rotate only 360/n degree around the target object. However, the major drawback in using multiple SUSTs is that all of them cannot be placed experimentally at same distance from the scanning center. Each of them rotates around the sample in concentric circles with slight difference in radius (~ 1-3 mm). This problem doesn't exist in case of full-ring array transducers as each sensor element is exactly at same scanning radius. To reconstruct cross-sectional PA images, usually a simple delay-and-sum algorithm implementing back-projection technique is used. This algorithm requires scanning radius as input from the user. Conventionally, trial-and-error method is being used to find out the scanning radius. Since it involves human expertise to figure out, this method is inefficient and time-taking. Only one reconstruction radius is to be found for circular array transducers and single-SUST based PACT systems. But in multi-SUST PACT system, each SUST radius has to be found out because if a single radius is used for the combined PA data from all SUSTs, the target image is imperfectly reconstructed. The PA image looks distorted. As 'n' increases, this distortion also increases. By using individual SUST radius, the target object can be perfectly reconstructed. Conventional trial-and-error method to find these scanning radii is cumbersome. To circumvent this difficulty, there is a need to automation of finding the reconstruction radius for all SUSTs in a circular scanning multi-SUST PACT system.

In this work, we propose a simple calibration method to find automatically the scanning radius of each SUST. We also demonstrate the importance of using different scanning radii for each SUST in a multi-SUST PACT system scenario. The efficacy of the proposed method is shown by using a derenzo numerical phantom. We have also experimentally validated this method using a point target phantom. To compare the quality of the reconstructed PA images, Pearson Correlation Coefficient (PCC) metric was used for numerical phantom and signal to noise ratio (SNR) was used for experimental phantom.

Table 1. Sensor specifications

Transducer #	Radius (mm)	SNR (dB)	Bandwidth (%)	Sensitivity (%)
SUST1	40	40	70	100
SUST2	41	31	68	97
SUST3	37	25	72	95
SUST4	43	37	74	94
SUST5	39	34	66	93
SUST6	42	26	71	96
SUST7	38	28	69	92
SUST8	40	32	73	91

2. MATERIAL AND METHODS

2.1 Numerical simulations

k-wave toolbox [30] in MATLAB was used for all numerical simulations. The computation grid consists of 900 X 900 pixels (0.1 mm/pixel) surrounded by a perfectly matched boundary layer. Different parameter specifications for sensors SUST1 to SUST8 are shown in Table 1. All transducers have central frequency of 2.25 MHz and 13 mm diameter active area. We have simulated the PA data with different scanning radius for each SUST in order to replicate the real-time scenario where each transducer rotates around the sample in different radius. We have also used different bandwidths, SNR levels and sensitivity for each transducer as shown in Table 1. A derenzo numerical phantom was used [Fig. 1(c)]. In case of 2-SUST PACT system (n = 2) scenario, SUST1 and SUST2 were used for acquiring PA data at 100 sensor location each. In case of 4-SUST PACT system (n = 4) scenario SUST1 to SUST4 were used (each 50 detector

locations), similarly for 8-SUST PACT system (n = 8) configuration SUST1 to SUST8 (each 25 sensor locations) were used. All the simulate PA data were generated with a time step size of 40 ns and a total of 1350 time steps for derenzo numerical phantom. The reconstructed PA images in all these scenarios were compared with that of images obtained for single-SUST PACT system scenario where SUST1 (200 detecting locations) was used.

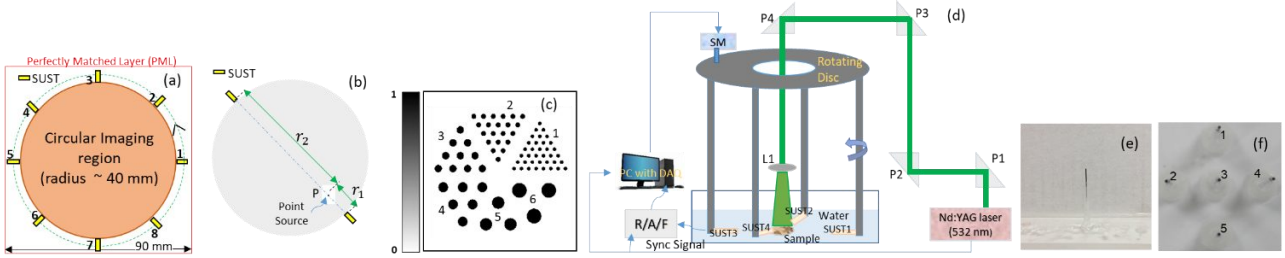

Fig. 1 (a) Schematic diagram of *k*-wave simulation geometry in MATLAB. Computational grid of 900 X 900 pixels (0.1 mm/pixel) was used in all simulations. SUST: Single-element Ultrasound Transducer (b) Calibration method using a point source 'P' at (550,550), r_1 nearest and r_2 farthest distances between point source 'P' and the transducer (c) derenzo phantom (d) schematic of the experimental set up with four transducers, R/A/F: receiver, amplifier, filter; SM: stepper motor; P1, P2, P3: right angle prisms; L1: Plano-concave lens; DAQ: data acquisition card, SUST1-SUST4: four single-element ultrasound transducers. (e) single point source phantom used for calibrating radius (f) five point target phantom.

2.2 Calibration Method

A single-element transducer collects time-resolved PA signal called as A-line (here at 200 detecting location) around the target object in full circle in a photoacoustic tomographic imaging system. Consider an arbitrary point source 'P' [Fig. 1(b)]. The A-lines at each sensor location have a peak amplitude at a particular time step. These time steps at which peak amplitude is observed, gives us the distance between the point source 'P' and the sensor which can be calculated as:

$$distance\ (cm) = timestep * \frac{c}{f_s} \tag{1}$$

where c is the speed of sound in water (0.15 cm/μs) and f_s is the sampling frequency (25 MHz). The point source will be closest to the transducer at say r_1 distance at one of the sensor locations and will be farthest at another diametrically opposite location say r_2 as shown in Fig. 1(b). Therefore, the reconstruction radius (r) can be calculated as:

$$r = \frac{r_1 + r_2}{2} \tag{2}$$

A MATLAB code was written to implement this algorithm. A point source was considered at (550,550) pixel location and for each transducer SUST1 to SUST8 the reconstruction radius was calibrated by using the proposed method and found to be 40.08 mm, 41.10 mm, 37.05 mm, 43.02 mm, 39.03 mm, 42.06 mm, 38.04 mm and 40.08 mm respectively. These calibrated radii were perfectly matching with the simulated ideal radius of each SUST (Table 1) with a negligible error of 0.05 – 0.24%. This radius calibration for each SUST needs to be done only once for any transducer configuration. Later the same radius can be used for reconstructing the PA images of any target phantom.

2.3 Experimental method

The experimental schematic set up is shown in Fig. 1(d). Laser pulses (5 ns pulse width, 10 Hz repetition rate at 532 nm wavelength) from a Q-switched Nd:YAG laser were delivered on to the sample using three right angled prisms and one Plano-concave lens. The optical fluency maintained was around ~ 9 mJ/cm^2 within the ANSI safety limits [31]. Four SUSTs [SUST1 to SUST4 as shown in Fig. 1(d)] of 2.25 MHz central frequency with 13 mm diameter active area with ~ 70% nominal bandwidth (Olympus NDT, V306-SU) were used for acquisition of PA data. The reconstruction radius for all these four SUSTs were found by using the proposed calibration method. Initially, once the transducers were mounted, a point source made of pencil lead (0.5 mm diameter) held using pipette tube adhered on acrylic slab [Fig. 1(e)] was placed in an arbitrary location in the imaging region. The PA signals were collected around the sample in full 360 degree

with all four transducers for 480s with a rotational speed of 0.75 degree/sec. The acquired PA signals were averaged into 100 A-lines. From these A-lines, the reconstruction radius for each SUST was computed using the proposed algorithm. The reconstruction radii for SUST1 to SUST4 were found to be 71.82 mm, 72.96 mm, 71.16 mm and 69.12 mm respectively. Then to experimentally validate the proposed method, we have used a five point target phantom [Fig. 1(f)] consisting of one pencil lead placed at scanning center and others at ~ 1 cm from the scanning center. We have compared the quality of the images obtained using multi-SUST system [each transducer collects 300 A-lines (n=2); and 150 A-lines (n=4)] with that of the images obtained using single-SUST PACT system (600 A-lines) after reconstructing the PA data using these calibrated radii. In all these scenarios the SUSTs were rotating at speed of 3 degree/sec. All the acquired PA signals were recorded using a data acquisition card (Spectrum, M2i.4932-exp) inside a desktop after amplification and filtering by a pulse amplifier (Olympus-NDT, 5072PR). Modified delay-and-sum algorithm was used in all the reconstructions for numerical and experimental data [11].

3. RESULTS AND DISCUSSION

Figure 2 shows the reconstructed PA images for derenzo numerical phantom. The reconstructed PA image of derenzo phantom obtained using SUST1 for a full 2π rad is shown in Fig. 2(a). The reconstructed PA images obtained for 2-SUST PACT scenario are shown in Figs. 2(b, c, d). Figure 2(b) shows the reconstructed PA image obtained using SUST1 from 0^0 to 180^0 around the target phantom. Figures 2(c) and (d) show the reconstructed PA images for the combined PA data from SUST1 and SUST2 without and with radius compensation respectively. Similarly, for 4-SUST PACT and 8-SUST PACT system configurations the reconstructed PA images are represented in Figs. 2(e, f, g) and 2(h, i, j), respectively. The acquired PA data for each SUST was only 180^0, 90^0, 45^0 in case of 2, 4, 8-SUST scenarios. Hence, the target object information contains small artefacts (blurring) as shown by red arrow marks in Fig. 2(b). All the circular objects were not reconstructed in Figs. 2(e, h) (red arrow marks) as compared to Fig. 2(a). This is the limited view problem [32] which can be avoided by using multiple SUSTs. The target image was not perfectly reconstructed when a single reconstruction radius was used for all transducers in all the configurations (n = 2, 4, 8) as shown in Figs. 2(c, f, i). This distortion in the reconstructed PA image was high in case of 8-SUST compared to 4-SUST and 2-SUST scenarios. By using individual reconstruction radius for each SUST calibrated from the proposed method, the shape of the circular objects was preserved as can be observed in Figs. 2(d, g, j). The quality of the images obtained for 2, 4, 8-SUST PACT systems were compared with that of the images obtained for single-SUST PACT system using PCC values. The PCC values for multi-SUST PACT scenarios were 0.63 for 2-SUSTs, 0.63 for 4-SUSTs and 0.60 for 8-SUST PACT system scenarios. These values were matching with that of the PCC value (0.62) in case of single-SUST PACT configuration.

Next, we have verified the feasibility of the proposed calibration method for real time experiments with a point source phantom [Fig. 1(f)]. Figure 3 shows the reconstructed cross-sectional PA images of five points. The reconstructed PA image for single-SUST PACT system scenario (SUST1 [Fig. 1(d)] rotating in 360^0) is shown in Fig. 3(a). For 2-SUST PACT system scenario (each transducer collecting the PA data only for 180^0), the reconstructed PA images are represented in Figs. 3(b, c, d). The reconstructed PA image obtained using SUST1 [Fig. 1(d)] acquiring the PA data from 0^0 to 180^0 is shown in Fig. 3(b). Figures 3(c, d) represent the cross sectional reconstructed PA images for the combined PA data from SUST1 (0^0 to 180^0) and SUST3 (180^0 to 360^0) [Fig. 1(d)] without and with radius compensation, respectively. Similarly, Figs. 3(e, f, g) represent the reconstructed PA images for 4-SUST PACT system. Figure 3(e) represents the reconstructed image obtained for SUST1 (0^0 to 90^0). Figure 3(f) represents the reconstructed PA image using single reconstruction radius (here SUST1 radius) for the combined PA data obtained using SUST1 to SUST4 [Fig. 1(d)], each rotating 90^0 around the sample. Figure 3(g) represents the reconstructed PA image obtained for combined PA data from all transducers SUST1 to SUST4 [Fig. 1(d)] using calibrated reconstruction radius (computed for single point target using proposed method) for each SUST data. Due to limited rotation of the transducers in 180^0, 90^0 in case of 2 and 4 SUST based PACT system scenarios, the point targets were not perfectly reconstructed as shown in Figs. 3(b, e) compared to Fig. 3(a). This is the limited data problem [32] in photoacoustic and thermoacoustic tomography where the transducer doesn't collect the information around the sample in full 360^0. To circumvent this problem, multiple SUSTs can be employed to collect data around the sample in full 360 degree. By reconstructing the PA data (using single reconstruction radius) collected from all transducers in each of the 2, 4-SUST based PACT configurations, the target

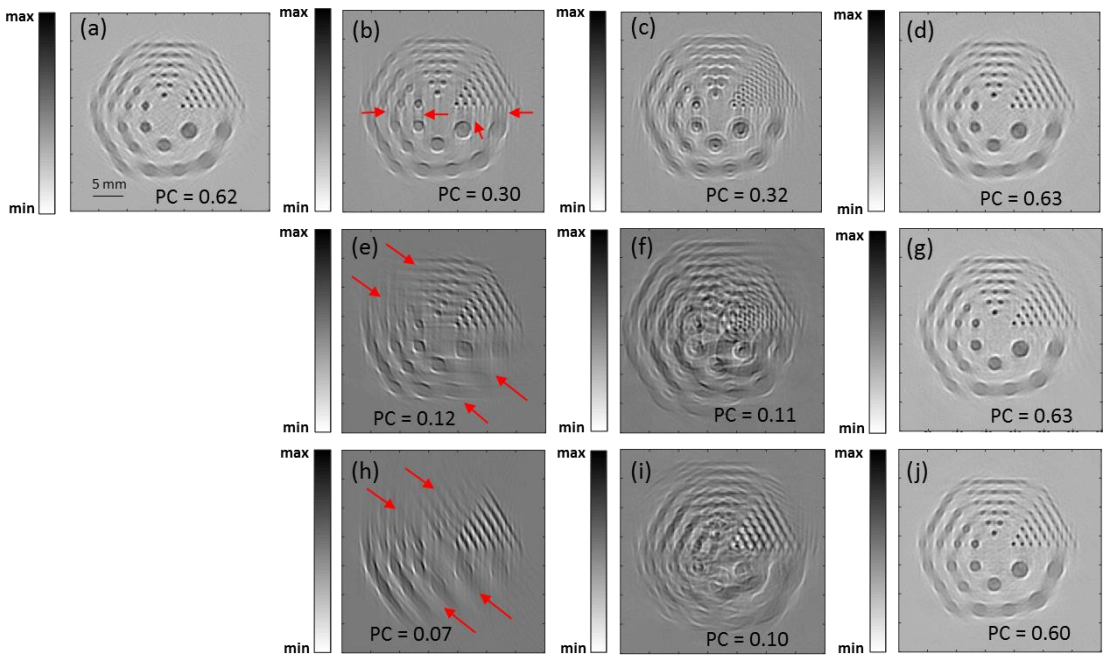

Fig. 2 Cross-sectional reconstructed PA images of derenzo numerical phantom for configurations of (a) single-SUST PACT system (b-d) 2-SUST PACT system, (e-g) 4-SUST PACT system and (h-j) 8-SUST PACT system: (b, e, h) reconstructed PA image for SUST1 from 0^0 to 180^0, 0^0 to 90^0 and 0^0 to 45^0 respectively, (c, d) reconstructed PA image for combined PA data using SUST1 and SUST3 (each rotating 180^0) without and with radius compensation respectively, (f, g) reconstructed PA image for combined PA data using SUST1-SUST4 (each rotating 90^0) without and with radius compensation respectively, (i, j) reconstructed PA image for combined PA data using SUST1-SUST8 (each rotating 45^0) without and with radius compensation respectively. Corresponding PCC values are shown at the bottom in each image. Color bar is shown for all images on the left. Scale bar is shown in (a).

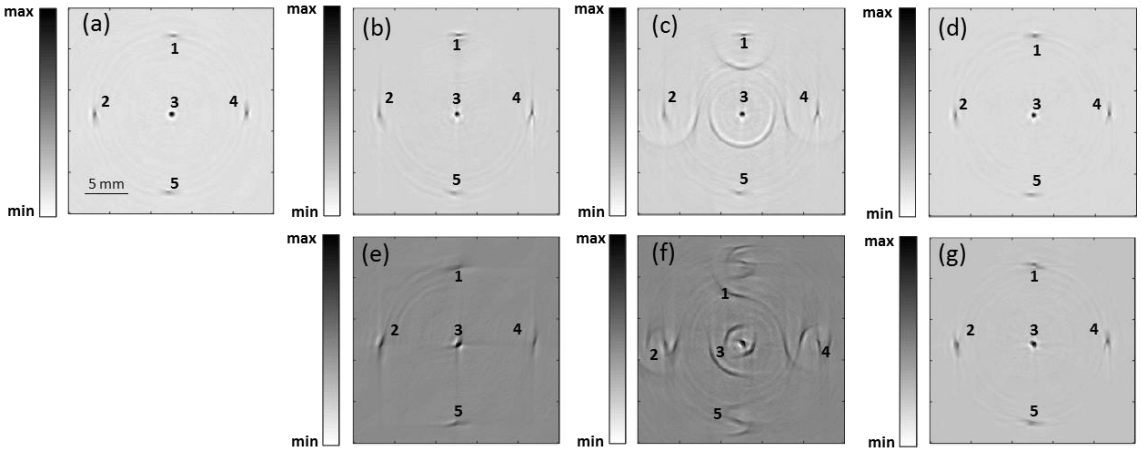

Fig. 3 Cross-sectional reconstructed PA images of point source phantom for configurations of (a) single-SUST PACT system (b-d) 2-SUST PACT system and (e-g) 4-SUST PACT system: (b, e) reconstructed PA image for SUST1 from 0^0 to 180^0 and 0^0 to 90^0 respectively, (c, d) reconstructed PA image for combined PA data using SUST1 and SUST3 (each rotating 180^0) without and with radius compensation respectively, (f, g) reconstructed PA image for combined PA data using SUST1-SUST4 (each rotating 90^0) without and with radius compensation respectively. Color bar is shown for all images on the left. Scale bar is shown in (a).

phantom looks distorted as can be clearly seen in Figs. 3(c, f). This distortion was high for 4-SUST scenario compared to 2-SUST scenario. By using corresponding calibrated reconstruction radius for each SUST (calculated using the single point target [Fig. 1(e)]), the target phantom can be perfectly reconstructed as evident in Figs. 3(d, g) similar to that in Fig. 3(a). To compare the quality of the reconstructed images SNR was calculated for point target phantom. It was observed that the SNR values for multi-SUST PACT scenarios (33.41 dB for 2-SUSTs, 33.27 dB for 4-SUSTs) were similar to that of the SNR value of 33.35 dB for single-SUST PACT configuration.

3. CONCLUSIONS

In a delay-and-sum reconstruction algorithm, the reconstruction radius is as an important parameter for obtaining perfectly reconstructed target image. In this work, we proposed an algorithm to calibrate this scanning radius for a single-element ultrasound transducer in circular scanning PACT system. This circumvents the limitations in conventional trial-and-error method to find the reconstruction radius. This calibration method is very helpful in a circular scanning multi-SUST based PACT system as each individual SUST data requires the corresponding scanning radius for obtaining perfect reconstruction of PA images. We have demonstrates the effectiveness of the proposed method using a derenzo numerical phantoms) in case of 2, 4, and 8 – SUST PACT system configurations. The quality of the images obtained for these scenarios were similar in terms of PCC metric values with that of single-SUST based PACT system. We have also demonstrated the feasibility of the this calibration method for experimental data of a five-points target phantom in case of 2, 4-SUST based PACT systems. The SNR levels of the reconstructed PA images obtained for these configurations were similar to that of the single-SUST PACT system.

ACKNOWLEDGEMENT

This research was supported by the financial support from the Singapore National Research Foundation administered by the Singapore Ministry of Health's National Medical Research Council (NMRC/OFIRG/0005/2016: M4062012). Authors have no relevant financial interests in the manuscript and no other potential conflicts of interest to disclose.

REFERENCES

[1] P. K. Upputuri, and M. Pramanik, "Recent advances toward preclinical and clinical translation of photoacoustic tomography: a review," Journal of Biomedical Optics, 22(4), 041006 (2017).
[2] A. Taruttis, and V. Ntziachristos, "Advances in real-time multispectral optoacoustic imaging and its applications," Nature Photonics, 9(4), 219-227 (2015).
[3] L. Li, L. Zhu, C. Ma *et al*., "Single-impulse panoramic photoacoustic computed tomography of small-animal whole-body dynamics at high spatiotemporal resolution," Nature Biomedical Engineering, 1, 0071 (2017).
[4] Y. Zhou, J. Yao, and L. V. Wang, "Tutorial on photoacoustic tomography," Journal of Biomedical Optics, 21(6), 061007 (2016).
[5] L. V. Wang, and J. Yao, "A practical guide to photoacoustic tomography in the life sciences," Nature Methods, 13(8), 627-38 (2016).
[6] L. V. Wang, "Multiscale photoacoustic microscopy and computed tomography," Nature Photonics, 3(9), 503-509 (2009).
[7] L. V. Wang, and S. Hu, "Photoacoustic Tomography: In Vivo Imaging from Organelles to Organs," Science, 335(6075), 1458-1462 (2012).
[8] L. V. Wang, "Prospects of photoacoustic tomography," Medical Physics, 35(12), 5758-67 (2008).
[9] S. Gutta, V. S. Kadimesetty, S. K. Kalva *et al*., "Deep neural network-based bandwidth enhancement of photoacoustic data," Journal of Biomedical Optics, 22(11), 116001 (2017).
[10]S. Gutta, M. Bhatt, S. K. Kalva *et al*., "Modeling errors compensation with total least squares for limited data photoacoustic tomography," IEEE Journal of Selected Topics in Quantum Electronics, (2017).

[11]S. K. Kalva, and M. Pramanik, "Experimental validation of tangential resolution improvement in photoacoustic tomography using a modified delay-and-sum reconstruction algorithm," Journal of Biomedical Optics, 21(8), 086011 (2016).
[12]M. Pramanik, "Improving tangential resolution with a modified delay-and-sum reconstruction algorithm in photoacoustic and thermoacoustic tomography," Journal of the Optical Society of America A, 31(3), 621-7 (2014).
[13]M. Xu, and L. V. Wang, "Universal back-projection algorithm for photoacoustic computed tomography," Physical Review E, 71(1), 016706 (2005).
[14]J. Prakash, A. S. Raju, C. B. Shaw *et al.*, "Basis pursuit deconvolution for improving model-based reconstructed images in photoacoustic tomography," Biomed Opt Express, 5(5), 1363-77 (2014).
[15]Y. Xu, D. Z. Feng, and L. V. Wang, "Exact frequency-domain reconstruction for thermoacoustic tomography - I: Planar geometry," IEEE Transactions on Medical Imaging, 21(7), 823-828 (2002).
[16]Y. Xu, M. H. Xu, and L. V. Wang, "Exact frequency-domain reconstruction for thermoacoustic tomography - II: Cylindrical geometry," IEEE Transactions on Medical Imaging, 21(7), 829-833 (2002).
[17]M. Jaeger, S. Schüpbach, A. Gertsch *et al.*, "Fourier reconstruction in optoacoustic imaging using truncated regularized inverse k-space interpolation," Inverse Problems, 23(6), S51-S63 (2007).
[18]T. T. Wong, R. Zhang, C. Zhang *et al.*, "Label-free automated three-dimensional imaging of whole organs by microtomy-assisted photoacoustic microscopy," Nature Communications, 8(1), 1386 (2017).
[19]J. Yao, J. Xia, and L. V. Wang, "Multiscale Functional and Molecular Photoacoustic Tomography," Ultrason Imaging, 38(1), 44-62 (2016).
[20]A. Dima, and V. Ntziachristos, "In-vivo handheld optoacoustic tomography of the human thyroid," Photoacoustics, 4(2), 65-69 (2016).
[21]A. Dima, and V. Ntziachristos, "Non-invasive carotid imaging using optoacoustic tomography," Optics Express, 20(22), 25044-57 (2012).
[22]K. Sivasubramanian, V. Periyasamy, and M. Pramanik, "Non-invasive sentinel lymph node mapping and needle guidance using clinical handheld photoacoustic imaging system in small animal," Journal of Biophotonics, (2017 (In Press)).
[23]Y. Talukdar, P. Avti, J. Sun *et al.*, "Multimodal ultrasound-photoacoustic imaging of tissue engineering scaffolds and blood oxygen saturation in and around the scaffolds," Tissue Eng Part C Methods, 20(5), 440-9 (2014).
[24]E. W. Stein, K. Maslov, and L. V. Wang, "Noninvasive, in vivo imaging of blood-oxygenation dynamics within the mouse brain using photoacoustic microscopy," Journal of Biomedical Optics, 14(2), 020502 (2009).
[25]P. K. Upputuri, and M. Pramanik, "Dynamic in vivo imaging of small animal brain using pulsed laser diode based photoacoustic tomography system," Journal of Biomedical Optics Letters, (2017).
[26]M. Moothanchery, R. Z. Seeni, C. Xu *et al.*, "In vivo studies of transdermal nanoparticle delivery with microneedles using photoacoustic microscopy," Biomedical Optics Express, 8(12), 5483-5492 (2017).
[27]Y. Gawale, N. Adarsh, S. K. Kalva *et al.*, "Carbazole Linked NIR Aza-BODIPY Dyes as Triplet Sensitizers and Photoacoustic Contrast Agents for Deep Tissue Imaging," Chemistry - A European Journal, 23(27), 6570-6578 (2017).
[28]S. K. Kalva, and M. Pramanik, "Use of acoustic reflector to make compact photoacoustic tomography system," Journal of Biomedical Optics, 22(2), 026009 (2017).
[29]P. K. Upputuri, V. Periyasamy, S. K. Kalva *et al.*, "High-performance compact photoacoustic tomography system for in vivo small animal brain imaging," Journal of Visual Experiments (JoVE), (2017).
[30]B. E. Treeby, and B. T. Cox, "k-Wave: MATLAB toolbox for the simulation and reconstruction of photoacoustic wave fields," Journal of Biomedical Optics, 15(2), 021314 (2010).
[31][American National Standard for Safe Use of Lasers (ANSI Z136.1−2000)], (2000).
[32]Y. Xu, L. V. Wang, G. Ambartsoumian *et al.*, "Reconstructions in limited-view thermoacoustic tomography," Medical physics, 31(4), 724-733 (2004).